

---

# MINE.NETCD: A BENCHMARK FOR GLOBAL MINING CHANGE DETECTION ON REMOTE SENSING IMAGERY

---

A PREPRINT

Weikang Yu<sup>1,2</sup>, Xiaokang Zhang<sup>\*3</sup>, Xiao Xiang Zhu<sup>1,4</sup>, Richard Gloaguen<sup>2</sup>, Pedram Ghamisi<sup>2,5</sup>

<sup>1</sup>Technical University of Munich, 80333 Munich, Germany

<sup>2</sup>Helmholtz-Zentrum Dresden-Rossendorf (HZDR), 09599 Freiberg, Germany

<sup>3</sup>Wuhan University of Science and Technology, 430081 Wuhan, China

<sup>4</sup>Munich Center for Machine Learning, 80539 Munich, Germany

<sup>5</sup>Lancaster University, LA1 4YR Lancaster, U.K.

## ABSTRACT

Monitoring changes triggered by mining activities is crucial for industrial controlling, environmental management and regulatory compliance, yet it poses significant challenges due to the vast and often remote locations of mining sites. Remote sensing technologies have increasingly become indispensable to detect and analyze these changes over time. We thus introduce MineNetCD, a comprehensive benchmark designed for global mining change detection using remote sensing imagery. The benchmark comprises three key contributions. First, we establish a global mining change detection dataset featuring more than 70k paired patches of bi-temporal high-resolution remote sensing images and pixel-level annotations from 100 mining sites worldwide. Second, we develop a novel baseline model based on a change-aware Fast Fourier Transform (ChangeFFT) module, which enhances various backbones by leveraging essential spectrum components within features in the frequency domain and capturing the channel-wise correlation of bi-temporal feature differences to learn change-aware representations. Third, we construct a unified change detection (UCD) framework that integrates over 13 advanced change detection models. This framework is designed for streamlined and efficient processing, utilizing the cloud platform hosted by HuggingFace. Extensive experiments have been conducted to demonstrate the superiority of the proposed baseline model compared with 12 state-of-the-art change detection approaches. Empirical studies on modularized backbones comprehensively confirm the efficacy of different representation learners on change detection. This contribution represents significant advancements in the field of remote sensing and change detection, providing a robust resource for future research and applications in global mining monitoring. Dataset and Codes are available via the link.

**Keywords** Mining change detection, MineNetCD, global benchmark dataset, unified change detection framework, frequency domain learning, ChangeFFT, remote sensing, deep learning

## 1 Introduction

Mining operations are crucial to provide the materials required for infrastructure, technology, and wellbeing and ensure the energy transition but have significant environmental impacts [1]. Open-pit mine areas, where minerals are extracted from a pit in the ground, induce large excavations and produce massive wastes in the form of tailings and waste piles during their life cycle [2, 3]. These activities are closely linked to adverse impacts such as ecosystem fragmentation, degradation, geotechnical disasters, and biodiversity loss [4]. Land degradation is a primary concern due to mining-induced alterations such as excavations and the removal of topsoil and vegetation. This results in soil erosion, landscape instability, and ecosystem disruption [5, 6]. Sustainability aims to minimize environmental impact

---

\*Corresponding author

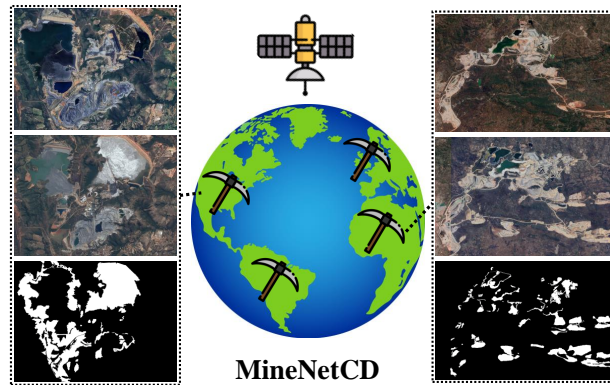


Figure 1: The MineNetCD.

and promote a better relationship between humans and our planet. While mining is inherently not sustainable, metal sourcing can be part of a sustainable society. Sourcing metals sustainably will require considering wellbeing as a purpose and preserving natural capital [7]. Sourcing the raw materials increasingly demanded by our societies will need transparent and inclusive stakeholder participation as well as a holistic understanding of the impact of extractive activities to reach sustainability status [8]. Geospatial data collected through satellite, drone, and aerial imagery plays a vital role in achieving metal sourcing sustainability by providing real-time, detailed perspectives on mining sites [9, 10]. Tools like machine learning and artificial intelligence (AI) help analyze this data to enhance the accuracy and speed of data analysis by transforming raw geospatial data into actionable insights [11]. This improved analysis enables better anticipation and mitigation of environmental risks, thereby reducing mining’s environmental footprint and aligning with the goals of AI for Social Good in building responsible AI [12]. Nowadays, remote sensing change detection technology using multitemporal images has become a key tool in tracking changes in the landscape caused by mining operations [13, 14, 15].

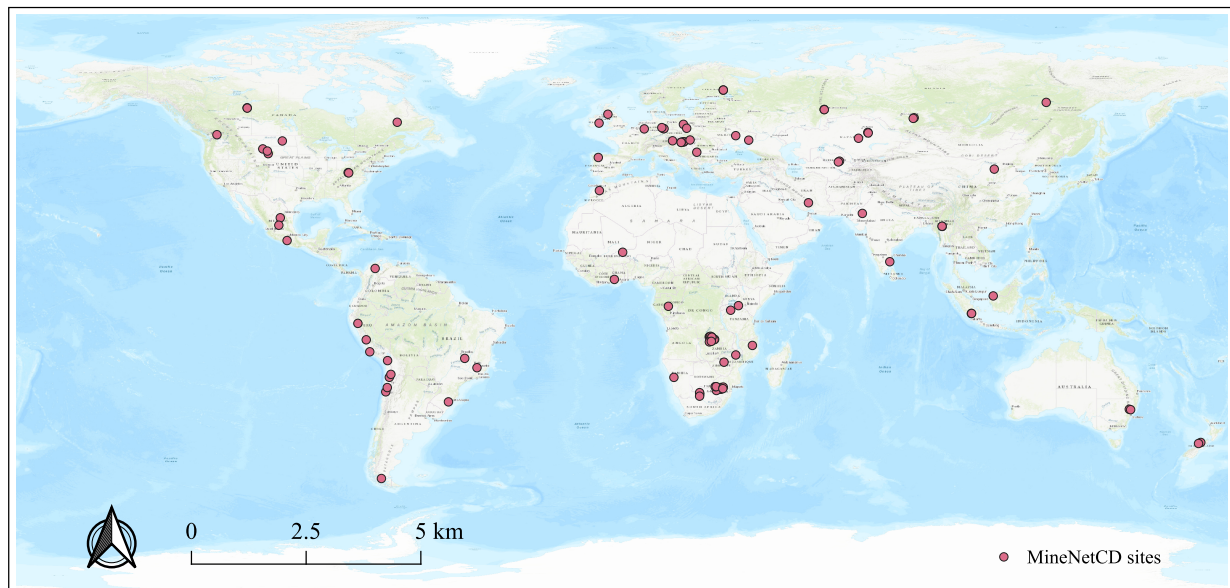


Figure 2: Spatial distribution of the mining sites in MineNetCD dataset

Mining change detection aims to quantify the changes caused by mining operations on the Earth’s surface by comparing the multitemporal images acquired in the same geographical areas [16, 17]. It is essentially a dense labeling task for pixel-wise classification. In recent years, deep learning-based methods have emerged as the dominant approach for change detection, leveraging encoder-decoder structures based on convolutional neural networks (CNNs) and transformers [18, 19]. Nevertheless, the success of these models heavily relies on large-scale, high-quality training

datasets, posing challenges in terms of data annotation and diversity. Li et al. [14] constructed the first open-pit mine change detection dataset, OMCD, with a resolution of 2 m containing bi-temporal images from 39 open-pit mining sites in China. On this basis, a CNN-based change detection method for open-pit mines has been investigated, in which the multiscale difference features of bi-temporal images were extracted and exploited by a Siamese network in an encoder-decoder structure [13]. To address the issue of data scarcity, Xie et al. [15] proposed a novel sub-instance data augmentation method based on a generative adversarial network to generate realistic and diverse samples.

For the change detection model, various strategies have been proposed to improve the feature representation of CNNs by leveraging multi-scale feature interaction [20, 21, 22, 23]. On this basis, attention mechanisms have been applied to refine feature maps along the spatial and channel dimensions [24, 25]. To handle the limitations of global context modeling in CNNs, recent methods have introduced transformers into change detection [26, 27]. They either take Transformer as their backbone or integrate it with CNNs to capture global contextual information [28, 29, 30]. Seeking to combine the strengths of CNNs and transformers, attention-based multiscale transformer networks have been investigated to extract global-local contextual information [31, 32, 33]. Overall, it is still challenging to model long-range contextual dependencies in an efficient manner while preserving the local details. Since mining change detection tasks focus on mining operation-driven land cover changes, the spectral variability poses more challenges to change-aware representation learning.

Open science has emerged as a vital paradigm in the development of artificial intelligence applications for Earth Observation (AI4EO), emphasizing transparency and the sharing of scientific research, data, and methodologies with the broader community. This involves not only disseminating final research outcomes but also sharing underlying data, models and codes. To streamline these processes, several open-source change detection frameworks<sup>2 3</sup> have been introduced, aiming to facilitate the application of various change detection methodologies on widely used datasets. However, these frameworks often require additional dataset preprocessing, and sharing pre-trained models remains cumbersome, leading to complex and repetitive operations. Additionally, the availability of datasets and trained model weights is limited, making it challenging to reproduce the results of different approaches. Consequently, current frameworks still demand a high level of specialized skills, setting a relatively high bar for researchers interested in this field.

In this paper, we attempt to build a benchmark for global mining change detection and to prompt the achievement of mining sustainability goals. The main contributions of this paper are summarized as follows:

- The global mining change detection dataset contains more than 70k paired patches of bi-temporal high-resolution remote sensing images and pixel-level annotations acquired from 100 mining sites worldwide.
- We developed a novel baseline model based on change-aware Fast Fourier Transform (ChangeFFT). It aids various backbones in leveraging key spectrum components within the features and capturing the channel-wise correlation of bitemporal features to learn the change-aware representations.
- A unified change detection framework (UCD) is constructed by integrating more than 13 advanced change detection models. It is designed for a more streamlined and efficient process, leveraging the cloud platform HuggingFace.

This paper is organized as follows. Section 2 describes the proposed mining change detection dataset. After that, a new baseline model and a new change detection framework are introduced in Section 3 and Section 4, respectively. The experimental performance is evaluated in Section 5. Finally, Section 6 concludes the paper.

## 2 MineNetCD Dataset

Utilizing artificial intelligence and deep learning for open-pit mining detection from remote sensing images has demonstrated its potential to enhance the precision of open-pit mining detection under various environmental conditions. Nevertheless, the success of these models heavily relies on large-scale, high-quality training datasets, posing challenges in terms of data annotation and diversity. The main challenges in constructing a global mining change detection dataset are twofold. First, it is difficult to accurately locate mining sites in countries worldwide, hindering image acquisition. Second, compared with other scenes, dense labeling of mining changes is more challenging due to the spectral similarity between mining areas and other ground objects, as well as the irregular shapes and fragmented boundaries of changed areas.

We sought to present a global high-resolution open-pit mining change detection dataset, MineNetCD. It has been recorded that more than six thousand active mining sites exist globally [3]. We intentionally selected 100 representative

<sup>2</sup><https://github.com/walking-shadow/Simple-Remote-Sensing-Change-Detection-Framework>

<sup>3</sup>[https://github.com/likyoo/change\\_detection\\_pytorch](https://github.com/likyoo/change_detection_pytorch)

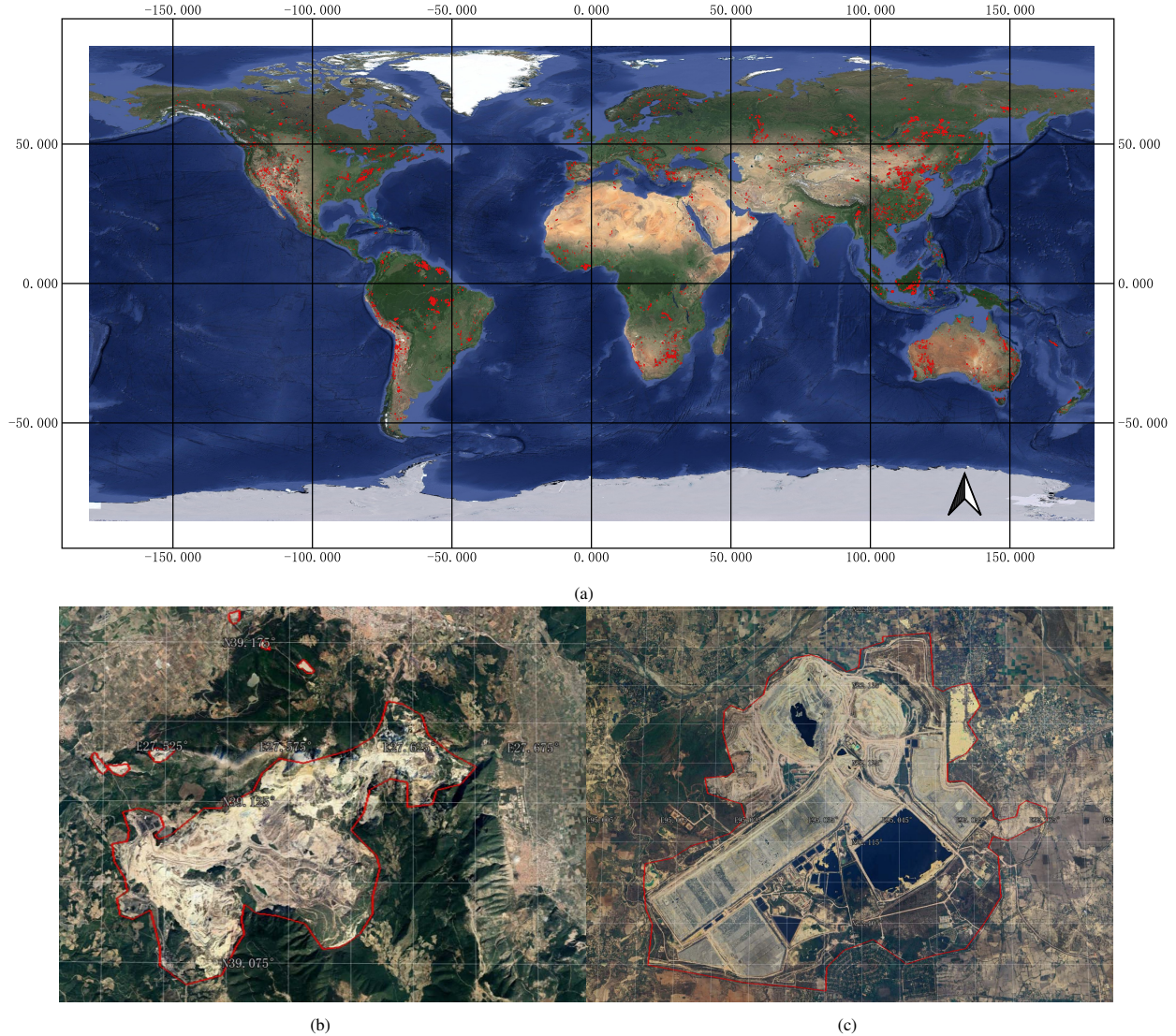


Figure 3: To locate the mining sites: (a) Overlay the global mining polygon data [3] onto Google Earth. This allows the sites to be accurately identified. (b) and (c) illustrate two such examples.

mining sites from different geographical regions to build the benchmark. The spatial distribution of mining sites in the MineNetCD dataset is illustrated in Fig. 2. The sites were chosen based on changes in the mining area and their spatial distribution. We aimed to capture representative mining locations from around the world. By overlaying the mining polygons onto remote sensing images, we can precisely locate the mining sites and retrieve the desired images, as shown in Fig. 3. This dataset has the following properties:

1. The largest: MineNetCD covers a wide range of open-pit mining sites located in different countries and regions across 6 continents. Each site involves bitemporal high-resolution imagery pairs with a spatial resolution of  $1.2m$  acquired via Google Earth Engine service. MineNetCD consists of more than 70k paired patches that have total coverage of approximately  $6756.88 \text{ km}^2$ .
2. High heterogeneity: The dataset includes bi-temporal image pairs that cover mining sites of various sizes, shapes, and industries. Additionally, the changes within the images are driven by multiple factors, leading to significant spectral heterogeneity and intensity variations. This high-diversity dataset allows for the evaluation of the generalization performance of change detection models. Some samples are displayed in Fig. 4. Fig. 5(a) depicts the number of mining sites per country, highlighting South Africa, Congo, and the USA as having the highest counts, with South Africa leading significantly. Fig. 5(b) quantifies the impacted land areas due

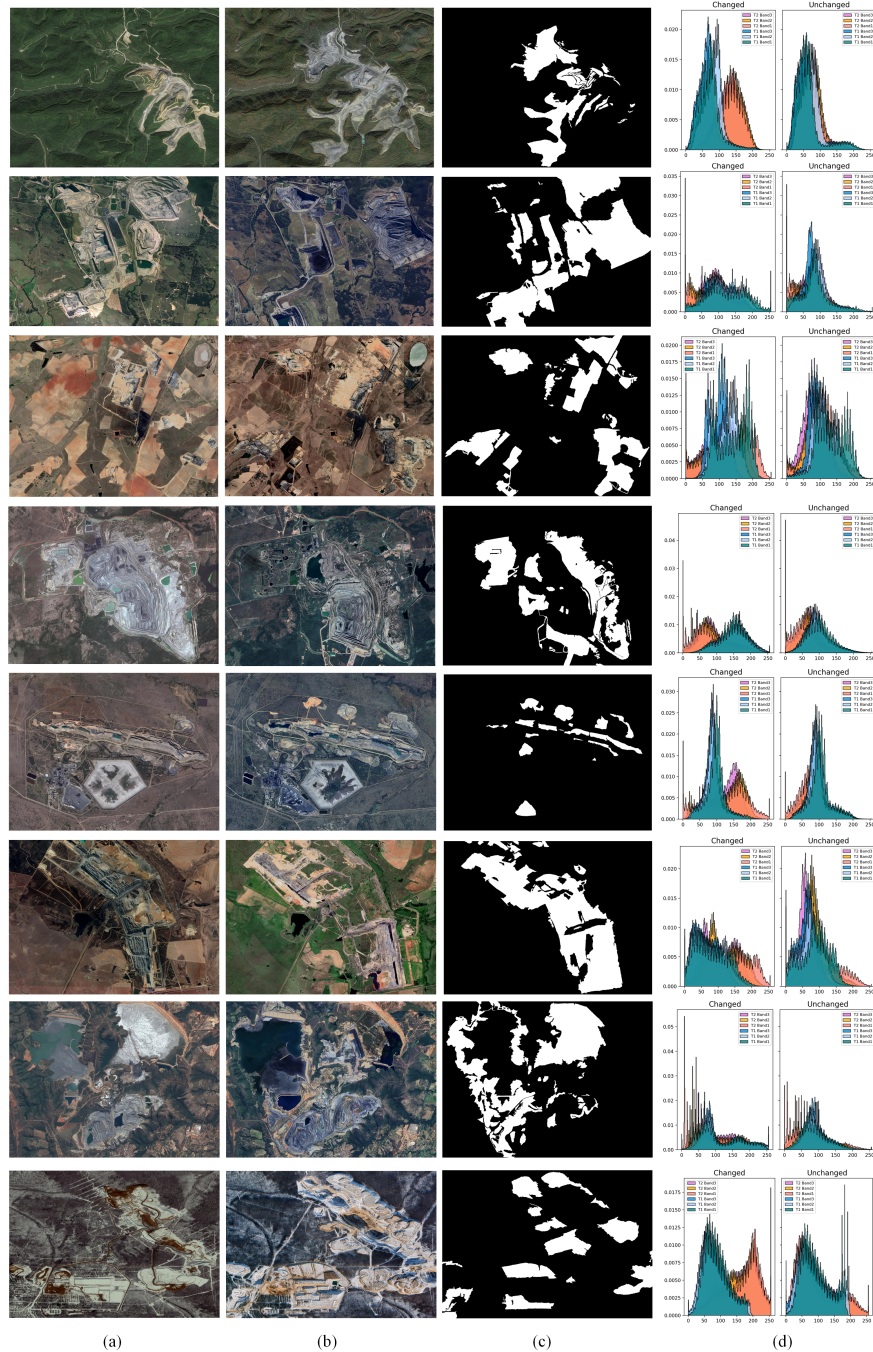


Figure 4: Typical samples in MineNetCD. (a) and (b) Pre- and post-event imagery. (c) Change masks. (d) Spectral intensity histograms.

to mining activities. Canada emerges as the most affected, with an extensive  $80km^2$  of altered landscape, followed by South Africa and Congo.

3. Towards mining-driven changes: Unlike current research that primarily focuses on urban or building-related changes [34, 24], this study examines land use/cover changes driven by mining operations, such as deforestation, erosion, and industrial expansion. Since land changes caused by mining are not frequent, the average time interval between the bi-temporal images is approximately 89.4 months or about seven years, with a minimum interval of four years to ensure an obvious change pattern exists in the mining areas. As shown

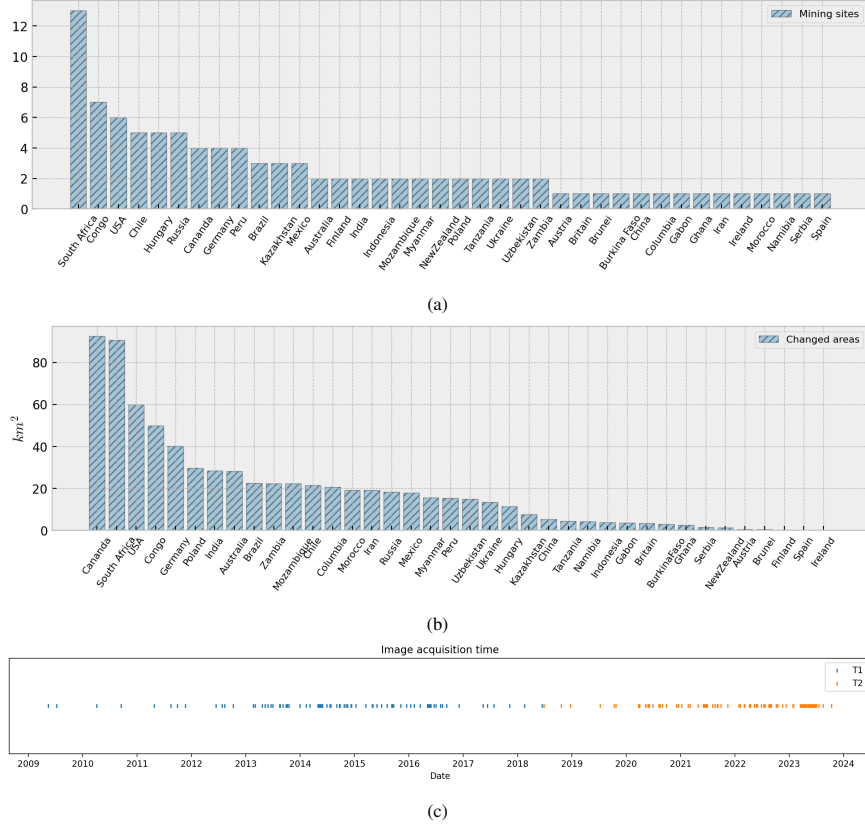


Figure 5: Statistics of MineNetCD. (a) No. of mining sites in each country. Changed areas of (b) each country and (c) each site. (d) Image acquisition time.

in Fig. 5(c), the acquisition time of the pre-change images ranges from 2009 to 2018, while the post-change images were taken from 2018 to 2023.

4. Fine-grained data: Semi-automatic labeling is employed for image annotations by utilizing the eCognition developer software. First, the segmentation map is created by co-segmenting the stacked bitemporal images using the fractal net evolution approach (FNEA) to generate spatially corresponding segments. Subsequently, image interpretation experts manually label the changed areas by comparing the pre- and post-change images. This process ultimately yields pixel-wise annotations with fine-grained boundaries. More details can be observed in Fig. 4.

### 3 MineNetCD Model

This section provides a detailed description of the proposed MineNetCD model, as shown in Fig 6. First, the bi-temporal images are forwarded into a modularized Siamese encoder with two weight-shared backbones to extract the multi-level bi-temporal deep features, which are then subtracted into feature differences. After that, a change-aware fast Fourier transform (ChangeFFT) module is incorporated to enhance the multi-level feature differences into change-aware representations with a frequency domain learning strategy. Consequently, the enhanced feature maps are processed by a UperNet-based change decoder to generate a change map, in which the multi-level features are progressively processed and upsampled with a pyramid pooling module (PPM) and a feature pyramid network (FPN).

#### 3.1 Modularized Siamese Encoder

In the literature, encoder-decoder-based change detection models typically use a fixed Siamese encoder to extract deep features from bitemporal images. This paradigm lacks scalability and adaptability for different change detection scenarios. To address this limitation, we propose a modularized Siamese encoder to build a more flexible change detection model. This encoder employs a weight-shared universal vision backbone with modularized representation

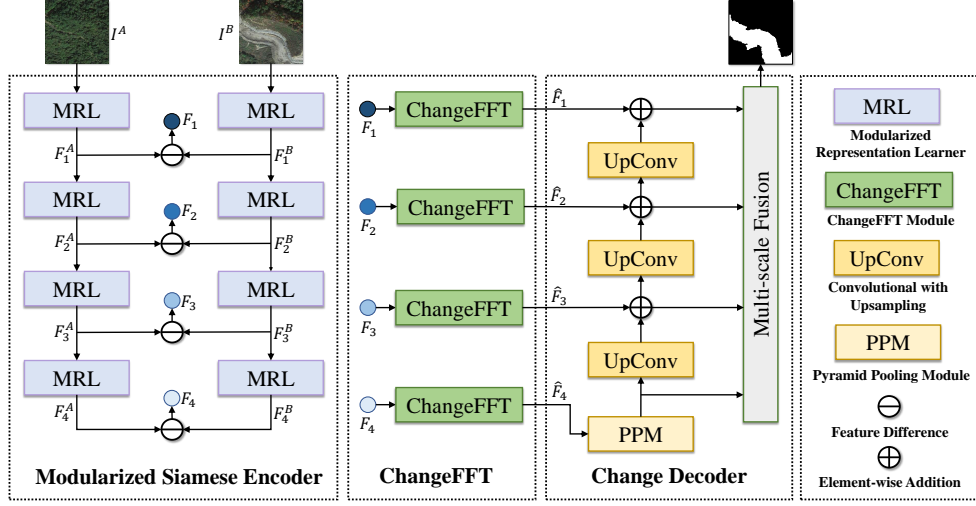


Figure 6: Proposed MineNetCD model for bi-temporal mining change detection.

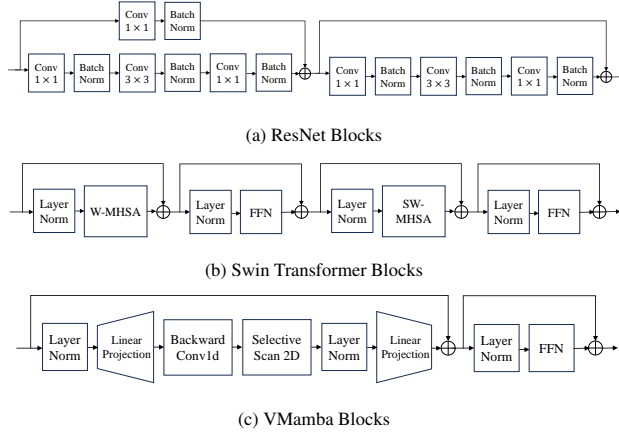


Figure 7: Illustration of different representation learners employed in the modularized Siamese encoder. The ResNet block consists of several convolutional layers with skip connections. The Swin-Transformer block utilizes a window multi-head self-attention (W-MHSA) and a subsequently shifted window multi-head self-attention (SW-MHSA) to capture the global dependencies and an MLP layer to enable channel-wise interactions. The VMamba block applies selective scan 2D to capture the contextual information and also an MLP layer for channel mixing.

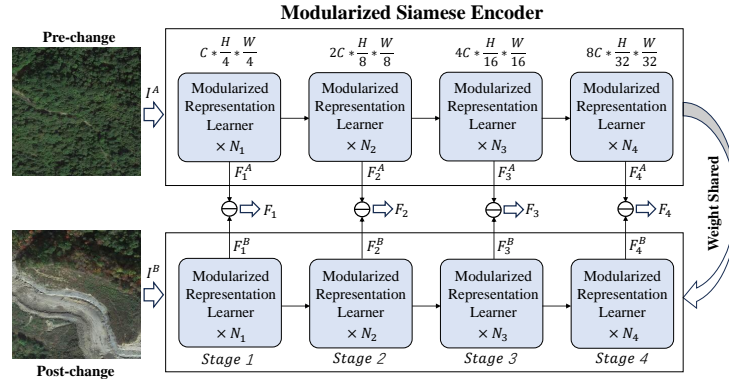


Figure 8: Illustration of the modularized Siamese encoder. The shapes of the output feature map of different levels are indicated on the top of the representation of learners.

Table 1: Overview of the backbone models adopted in this study.

Backbone Models	Learning Strategy	#Parameters	FLOPs
<i>ResNet Series</i>			
ResNet-18	CNN	11M	1.8G
ResNet-50		24M	3.8G
ResNet-101		43M	7.6G
<i>Swin Transformer Series</i>			
Swin-T	Transformers	28M	4.5G
Swin-S		50M	8.7G
Swin-B		88M	15.4G
<i>VMamba Series</i>			
VMamba-T	Mamba	30M	4.8G
VMamba-S		50M	8.7G
VMamba-B		89M	15.4G

learners that can be adjusted to different scales and incorporates various representation learning strategies. Consequently, our modularized Siamese encoder can adapt to heterogeneous remote sensing datasets with diverse scales and spectral characteristics.

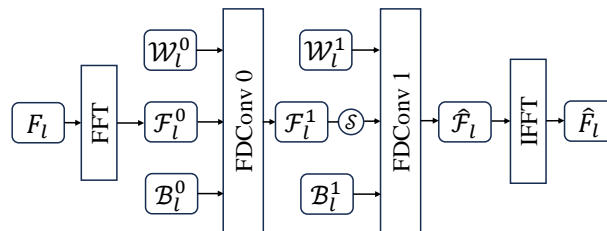
Over the past decade, numerous vision backbones have been developed to enhance the efficacy of learning deep representations. These backbones can be broadly categorized into Convolutional Neural Networks (CNNs), Transformer-based models, and Mamba-based models, reflecting their architecture and chronological development. As shown in Table 1, these backbones utilize convolutional networks, self-attention mechanisms, and selective state space models to learn deep representations, respectively. Furthermore, Fig. 7 illustrates the architectures of the representation learners in these backbones. Each type of backbone has a distinct focus: CNNs concentrate on localized image areas, self-attention models capture long-range dependencies among all feature elements, and selective state space models reduce computational complexity for context modeling with a selective scan 2D mechanism.

In this paper, we select one representative model for each type of backbone: ResNet [35] for CNNs, Swin Transformer [36] for transformer-based models, and VMamba [37] for Mamba-based models. These vision backbones consist of four stages of representation learners, and we construct a modularized weight-shared Siamese structure to integrate these models to extract bi-temporal features simultaneously from remote sensing images, as shown in Fig. 8. The  $N_1$ ,  $N_2$ ,  $N_3$ , and  $N_4$  denote the number of blocks of the modularized representation learners at each stage of the encoder, which can be adjusted to construct the backbones with different scales. Let  $I^A$  and  $I^B$  be the pre-change and post-change remote sensing images, the pre-change and post-change deep features of four different levels  $l = \{1, 2, 3, 4\}$  are extracted by the modularized Siamese encoder as  $\{F_l^A\}_{l=1}^4$  and  $\{F_l^B\}_{l=1}^4$ . After that, the multi-scale bi-temporal deep features are subtracted into feature differences  $\{F_l\}_{l=1}^4$  as follows:

$$F_l = F_l^A - F_l^B. \quad (1)$$

Since these vision backbones have been widely adopted in a range of AI4EO applications, our objective is to conduct a comprehensive evaluation of these backbones for remote sensing change detection and validate the effectiveness of the proposed ChangeFFT module on various representation learners. Furthermore, we select three variants with different scales of parameters for each vision backbone to evaluate their scalability in the change detection task.

### 3.2 Change-aware Fast Fourier Transform (ChangeFFT)

Figure 9: Illustration of the ChangeFFT module. The  $\mathcal{S}$  denotes SiLU activation function.



Currently, most encoder-decoder-based change detection approaches directly use feature differences as change representations to reconstruct a change map in the decoder. However, the subtraction operation for fusing bitemporal deep features can disrupt the well-learned deep representations due to the complex spatiotemporal relationships of the land surfaces, leading to challenges in distinguishing changes in the decoder. To overcome this challenge, we propose a change-aware Fast Fourier Transform (ChangeFFT) module that effectively learns change-aware representations from multi-level feature differences in the frequency domain.

Learning in the frequency domain has proven to be an efficient technique for capturing channel-wise dependencies of deep features [38]. By applying a Fast Fourier Transform (FFT), features are transformed from the time domain to the frequency domain, where change-aware representations can be precisely captured within the spectrum of feature differences. Let  $\{F_l\}_{l=1}^4 \in \mathbb{R}^{C_l \times H_l \times W_l}$  be the differenced features input, where  $C_l$ ,  $H_l$ , and  $W_l$  are the number of channels, height, and width of the  $l$ -th level of feature differences. The FFT can be calculated as follows:

$$\begin{aligned}\mathcal{F}_l(k) &= \int_D F(x)e^{-j2\pi kx} dx \\ &= \int_D F_l(x)\cos(2\pi kx)dx + j \int_D F_l(x)\sin(2\pi kx)dx \\ &= \mathcal{F}_l^R + j\mathcal{F}_l^I,\end{aligned}\tag{2}$$

where  $k$  is the frequency variable and  $x$  indexes the spatial coordinates.  $\mathcal{F}_l^R$  and  $\mathcal{F}_l^I$  is the real and imaginary part of the transformed feature  $\mathcal{F}_l$  at the  $l$ -th level, respectively. Subsequently, two convolutional layers are applied to enable a change-aware representation learning in the frequency domain. According to the convolutional theorem, the Fourier transform of a convolution of two tensors is the pointwise product of their Fourier transforms, as follows:

$$\text{FFT}\{H * G\} = \mathcal{H} \cdot \mathcal{G},\tag{3}$$

where  $*$  denotes the convolutional operator, and  $\mathcal{H}$  and  $\mathcal{G}$  are the Fourier transforms of tensors  $H$  and  $G$ , respectively. On this basis, a convolutional layer in the frequency domain (FDConv) can be initialized with learnable parameters  $\mathcal{W}$  and  $\mathcal{B}$  in complex representing the weights and biases, respectively. Let  $\mathcal{F}$  be a feature spectrum, the convolutional layer in the frequency domain can be computed as follows:

$$\begin{aligned}\text{FDConv}(\mathcal{F}) &= \text{FFT}(F * W + B) = \mathcal{F} \cdot \mathcal{W} + \mathcal{B}, \\ &= (\mathcal{F}^R \mathcal{W}^R - \mathcal{F}^I \mathcal{W}^I + \mathcal{B}_R) + j(\mathcal{F}^R \mathcal{W}^I + \mathcal{F}^I \mathcal{W}^R + \mathcal{B}_I),\end{aligned}\tag{4}$$

where the superscript  $R$  and  $I$  denote the real and imaginary components of a complex tensor, respectively. As shown in Fig. 9, we apply two consecutive FDConvs to ensure a comprehensive change-aware representation learning for each level of the feature differences.

The FDConv can be viewed as a channel attention mechanism that learns the attention weights from the spectrum of feature differences in the frequency domain, which can be more effective in representing the channel-wise features than the global average pooling used in the traditional squeeze-and-excitation channel attention block. In the meantime, the number of parameters of the ChangeFFT module for each level is restricted to the amount of  $C_l \cdot C_l + C_l$ , which is relatively lightweight compared with other complicated channel-wise feature enhancement methods like multi-level perception (MLP). Our calculation indicates that the incorporation of the ChangeFFT module will only increase by about 10% of the model parameters, indicating its ability to learn the change-aware representations in a balanced performance.

After the change-aware representation learning in two stages of FDConv, the obtained change representations are transformed back to the time domain with an inversed FFT (IFFT) function, as follows:

$$\begin{aligned}\hat{F}_l(x) &= \int_D \hat{\mathcal{F}}_l(k)e^{j2\pi kx} dk \\ &= \int_D (\hat{\mathcal{F}}_l^R(k) + j\hat{\mathcal{F}}_l^I(k))e^{j2\pi kx} dk,\end{aligned}\tag{5}$$

where  $\hat{\mathcal{F}}_l(k)$  is the spectrum output of the second stage of FDConv, as illustrated in Fig. 9.

Note that the FFT and IFFT are both performed along the channel dimension of the multi-scale features. In conclusion, the multi-level change-aware representations  $\{\hat{F}_l\}_{l=1}^4$  are obtained from feature differences  $\{F_l\}_{l=1}^4$  in the ChangeFFT module.

### 3.3 Change Decoder

To obtain a pixel-wise change map from the multi-scale change-aware representations, a multi-scale semantic decoder, named UperNet [39], is adopted that progressively fuses and upsample the multi-scale change-aware representations into a full-resolution change map. The UperNet has been widely employed as a plug-and-play semantic segmentor due to its superior compatibility with various vision backbones, which we considered also suitable for integrating with the modularized backbone and ChangeFFT module in this study.

The UperNet change decoder processes multi-scale change-aware representations through a hierarchical approach that combines a Pyramid Pooling Module (PPM) and a Feature Pyramid Network (FPN). Initially, the PPM extracts global context information by applying pooling operations at multiple scales to the deepest change representations, creating a set of pooled features that capture various levels of contextual information. These pooled features are then concatenated and upsampled to match the original resolution. Subsequently, the FPN aggregates features from different layers of the backbone network, progressively refining and merging them to produce high-resolution feature maps. These multi-scale features from the PPM and FPN are then fused to generate a comprehensive feature representation, which is finally passed through convolutional layers to produce the change map, effectively leveraging both local details and global context for accurate change detection.

### 3.4 Loss Function

We employ a pixel-wise binary cross-entropy (BCE) loss  $\mathcal{L}_{\text{BCE}}$  to train the MineNetCD model. The BCE loss measures the discrepancy between the predicted change probabilities and the ground truths for each pixel as follows:

$$\mathcal{L}_{\text{BCE}} = -\frac{1}{N} \sum_{i=1}^N [y_i \log(p_i) + (1 - y_i) \log(1 - p_i)], \quad (6)$$

where  $i$  indexes a pixel and  $N$  is the number of pixels.  $y_i$  denote a binary ground truth (0 for unchanged, 1 for changed) of pixel  $i$ , and  $p_i$  is the predicted probability that pixel  $i$  belongs to the changed class.

## 4 Unified Change Detection Framework

To promote deep learning-based change detection tasks for broader utilization by RS experts, we develop a unified change detection (UCD) framework based on the Huggingface platform with an open science prospect. The UCD framework currently includes more than 13 change detection approaches and 6 change detection datasets, including the MineNetCD dataset and model proposed in this paper. The UCD framework allows the user to simply specify the change detection method and dataset in the configuration file, on which the training and testing experiments can be automatically conducted without any professional skills. As a result, the change detection model can be initialized or loaded by using only one code line, respectively, as follows:

```
model=model.from_config(CONFIG)
model=model.from_pretrained(MODEL_ID)
```

where the CONFIG and MODEL\_ID are the model configurations and model paths, respectively. Furthermore, we leverage the Huggingface platform to facilitate the access of the dataset and model loading processes in a cloud-based paradigm. In particular, we uploaded the preprocessed datasets and pretrained model weights to the Huggingface Hub, which can be automatically loaded into the UCD framework by specifying their dataset and model ids in the configuration file. As a pioneer work, we have uploaded more than 70 model weights pretrained from 13 different approaches on 6 change detection datasets to our Huggingface Hub <https://huggingface.co/ericyu>. For future research, these pretrained models can be utilized to reproduce the results on these datasets, which avoids the efforts for re-training and maximizes the experiments' transparency.

The UCD is also designed with high compatibility that allows the users to easily integrate their own resources into the framework. We provide guidance and some tools for the users to preprocess and adapt their own datasets and models into standard formations that can be used in the UCD framework. We hope this new approach to the UCD framework will motivate future change detection researchers to participate in these open science activities, as well as provide an opportunity for everyone with an interest to have a try in change detection without any professional skills.

Table 2: Quantitative Comparisons in terms of OA, Pre, Rec, F1, and cIoU on MineNetCD dataset. The best and second-best results are highlighted in red and blue, respectively.

Methods	OA	Recall	Precision	F1	cIoU
A2Net	<b>0.9188</b>	<b>0.7218</b>	0.5766	<b>0.6410</b>	<b>0.4718</b>
BIT	0.9118	0.6732	<b>0.5804</b>	0.6233	0.4528
DMINet	0.8967	0.6266	0.4412	0.5177	0.3493
RDPNet	0.8774	0.5128	0.4818	0.4968	0.3305
ICIFNet	0.8920	0.5966	0.4342	0.5024	0.3356
SNUNet	0.8927	0.5829	0.5124	0.5452	0.3750
ChangeFormer	0.8705	0.4857	0.516	0.5003	0.3337
SiamUnet-Conc	0.8984	0.6469	0.4220	0.5108	0.3430
SiamUnet-Diff	0.8960	<b>0.7679</b>	0.2478	0.3746	0.2305
ResUnet	0.8671	0.4753	0.5512	0.5104	0.3427
FC-EF	0.8836	0.5628	0.3293	0.4154	0.2622
FCNPP	0.8559	0.4022	0.3024	0.3452	0.2087
MineNetCD (Ours)	<b>0.9251</b>	0.7120	<b>0.6814</b>	<b>0.6963</b>	<b>0.5343</b>

## 5 Experiments

### 5.1 Dataset Preparation

To facilitate the training and testing of the baseline models, the bi-temporal remote sensing image pairs from MineNetCD are cropped into a size of  $256 \times 256$ . We randomly selected 60%, 10%, and 30% of mining sites as the training, validation, and testing sets, respectively. For computation convenience, the bi-temporal images and labels are cropped into patches of size  $256 \times 256$ . Finally, the training, testing, and validation sets include a total of 47, 743, 19, 355, and 4, 613 patches, respectively.

In accordance with the open-science paradigm of the proposed UCD framework, the MineNetCD dataset can be easily accessed and integrated into the framework via <https://huggingface.co/datasets/ericyu/MineNetCD256>.

### 5.2 Baseline Approaches

The proposed MineNetCD baseline model is compared against several state-of-the-art deep learning-based RS-CD methods: a lightweight network with progressive aggregation and supervised attention (A2Net) [40], a bitemporal image transformer (BIT) network [26], a transformer-based Siamese network for change detection (ChangeFormer) [28], a dual-branch multi-level inter-temporal network (DMINet) [23], fully convolutional siamese networks for change detection (FC-EF) [41], a fully convolutional network within pyramid pooling (FCNPP) [42], an intra-scale cross-interaction and inter-scale feature fusion network (ICIFNet) [43], a region detail preserving network (RDPNet) [44], a residual U-Net (ResUnet) [45], a fully convolutional Siamese concatenated U-Net (SiamUnet-Conc) [41], a fully convolutional Siamese difference U-Net (SiamUnet-Diff) [41], an integrated Siamese network and nested U-Net (SNUNet) [22].

### 5.3 Experimental Settings

The proposed MineNetCD model is implemented using the open-source *transformers* package [46] based on the UCD platform. For the model training, the Adam optimizer was adopted with an initial learning rate of  $1e-4$ , a momentum of 0.9, and parameters  $\beta_1, \beta_2$  as 0.9 and 0.99, respectively. The batch size was set to 32 for each GPU. In addition, we employ a cosine annealing scheduler that gradually reduces the learning rate to  $1e-7$  for better model convergence.

In our experiments, the hyper-parameters for the methods considered for comparison were set to the default values according to their original publications. To ensure the reproduction of the experiments, the random seed is set to 8888. All experiments were conducted with a High-performance computing (HPC) system with a 128-core CPU and 8 NVIDIA Tesla A100 GPUs (40GB of RAM). In addition, the Accelerate [47] package is adopted for fully sharded data-parallel computing to speed up the computational of the models in our multi-GPU environment.

## 5.4 Evaluation Metrics

For quantitative evaluation, we adopt five commonly used metrics: overall accuracy (OA), precision (Pre), recall (Rec), F1-score, and change-class Intersection over Union (cIoU). The OA represents the percentage of pixels that are correctly detected among all samples. The precision is the number of correctly detected changed pixels divided by the number of all the pixels that are identified as changed in the change detection map. The recall is the percentage of correctly detected changed pixels among all the pixels that should be detected as changed. The F1-score is the harmonic mean of the precision and recall that also considers the class imbalance problem in change detection, and the cIoU reveals the exact coverage of the changed area of the detected change map compared with the ground truth. They are calculated according to the following equations:

$$OA = (TP + TN)/(TP + TN + FP + FN) \quad (7)$$

$$Pre = TP/(TP + FP), \quad (8)$$

$$Rec = TP/(TP + FN), \quad (9)$$

$$F1 = 2TP/(2TP + FP + FN), \quad (10)$$

$$cIoU = TP/(TP + FP + FN), \quad (11)$$

where the TP is the number of correctly detected changed pixels, TN is the number of correctly detected unchanged pixels, FP is the number of false alarms, and FN is the number of missed change pixels.

## 5.5 Benchmark Results with the State-of-the-art

### 5.5.1 Quantitative Results

Table 2 displays the quantitative evaluation comparisons of different methods in terms of OA, Precision, Recall, F1 score, and cIoU on the MineNetCD dataset. The results indicate that the MineNetCD dataset is challenging for current change detection methods, with an average F1 score of less than 0.65 and a cIoU of less than 0.48. Although some methods achieve promising recall values, they suffer from low precision, which leads to a lot of false alarms. On the contrary, the proposed model can achieve an F1 score of 0.6963 and a cIoU of 0.5343, which gains an improvement of at least 0.0553 and 0.0625 in terms of F1 score and cIoU, respectively, compared to all the competitors. The overall results demonstrate the effectiveness and superiority of the proposed MineNetCD model.

### 5.5.2 Qualitative Results

Fig. 10 and Fig. 11 show examples of MineNetCD results obtained using various comparative methods. Additionally, we present the results for original small patches sized  $256 \times 256$  to enable a comprehensive quantitative comparison. The visualizations reveal that most comparison methods struggle to accurately detect the correct changed areas while avoiding false alarms.

Based on these representative results, the proposed MineNetCD method demonstrates advantages in several aspects:

- **Better discrimination of changes:** In the first five rows of Fig. 12, most comparison methods fail to distinguish the changes in bi-temporal images, resulting in change maps with numerous omitted changes (false negatives, shown in blue). Conversely, the MineNetCD method consistently produces accurate change maps from these challenging samples, highlighting its superior ability to differentiate changes in bi-temporal images with heterogeneous spectral characteristics (e.g., rows one to three in Fig. 12) and subtle spectral differences (e.g., rows four and five in Fig. 12). This superior discrimination of the MineNetCD model is attributed to the ChangeFFT module, which aligns spatiotemporal feature differences by unifying their spectra in the frequency domain to obtain robust change-aware representations.
- **Fewer pseudo changes:** Compared to other methods, the MineNetCD model significantly reduces pseudo changes—false alarms or irrelevant changes to mining development. In Fig. 11, change maps generated by other methods exhibit extensive pseudo changes (denoted as red patches). In the two six of Fig. 12, most methods predict pseudo changes in mining areas already present in the pre-change image. In contrast, the change maps from the MineNetCD model exhibit fewer pseudo changes, benefiting from the ChangeFFT module’s ability to filter out noise in bi-temporal feature differences by processing their feature spectra in the frequency domain.
- **More precise boundaries:** Mining change detection often involves irregularly shaped instances due to the nature of open-pit mining developments. It is crucial to accurately capture the extent of the mining area. In Fig. 10 and rows eight to ten of Fig. 12, the change maps predicted by the comparison methods appear to have incorrect and unclear instance edges, while the MineNetCD model managed to capture precise edges

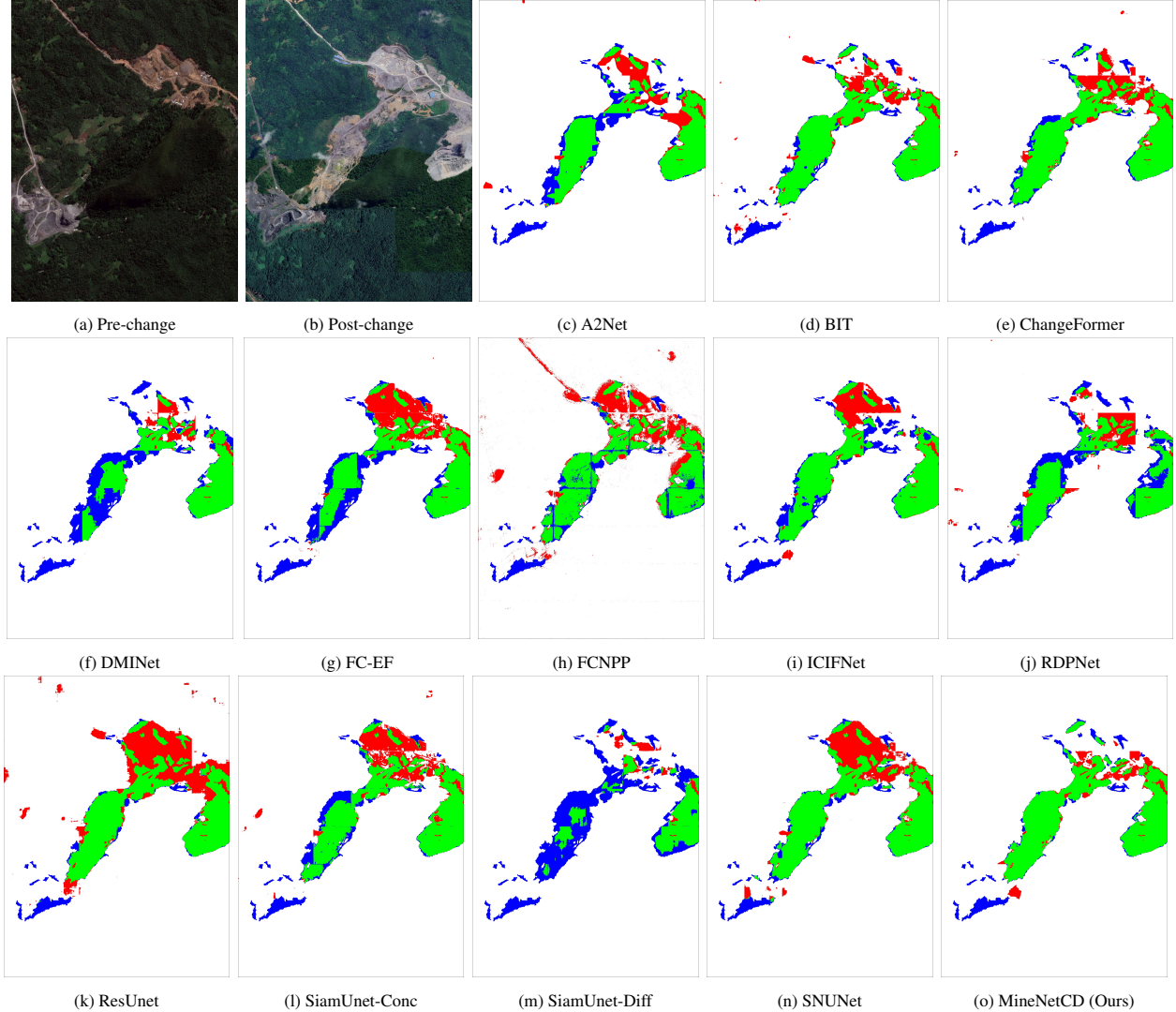


Figure 10: Visual comparisons of the proposed method and the state-of-the-art approaches on the MineNetCD dataset. The rendered colors represent true positives (green), true negatives (white), false positives (red), and false negatives (blue).

of change instances in mining areas. This precision is achieved through the change-aware representation learning in the ChangeFFT module, which accurately extracts spatiotemporal dependencies in the frequency domain.

The changes occurring in the benchmark set are very diverse and relevant for both the monitoring of the mining activities and their relevance for the environment and the local communities. The changes occur in the pits themselves, where extraction occurs, but also in the waste piles and tailings, where wastes are deposited, or the different processing units surrounding the mines. This is important because the impacts of mining vary from commodity to commodity, processing types, and environmental conditions. Only a holistic approach to mining changes can provide sufficient information to monitor and address the different impacts of mining sites.

## 5.6 Comparisons of Different Backbone Models for Change Detection

To explore the influence of different representation learners on the performance of change detection, we apply three distinct branches of backbone models, each with three variants at different scales, to build the modularized Siamese encoder of the MineNet model. As shown in Fig. 13, the Swin Transformer achieves the best performance on MineNetCD in terms of F1 score and cIoU among all the scales of the backbone variants. In particular, the high-

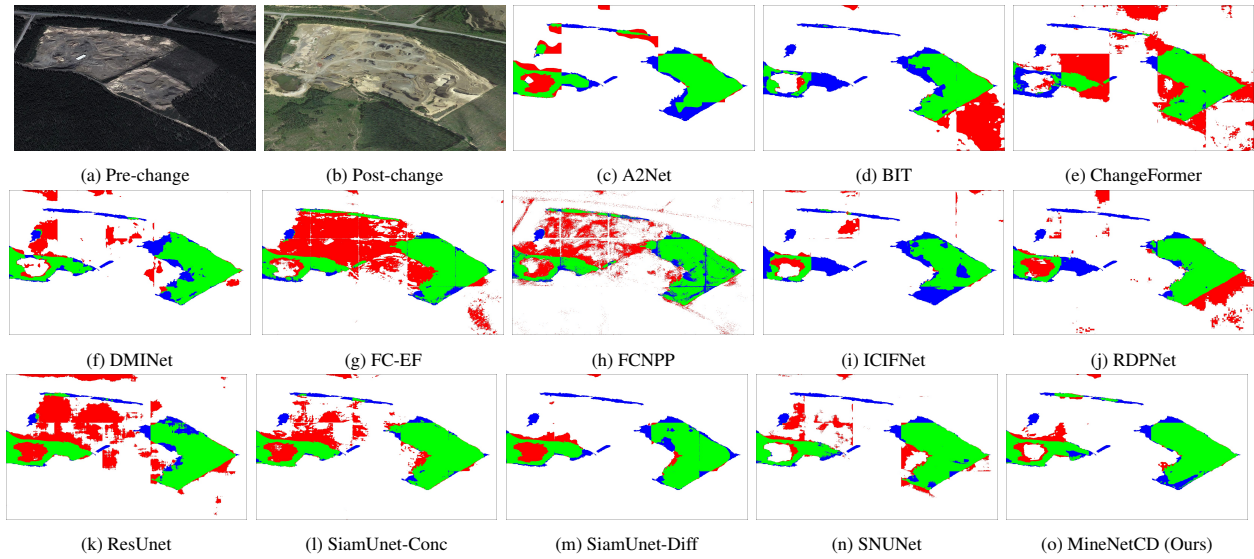


Figure 11: Visual comparisons of the proposed method and the state-of-the-art approaches on the MineNetCD dataset. The rendered colors represent true positives (green), true negatives (white), false positives (red), and false negatives (blue).

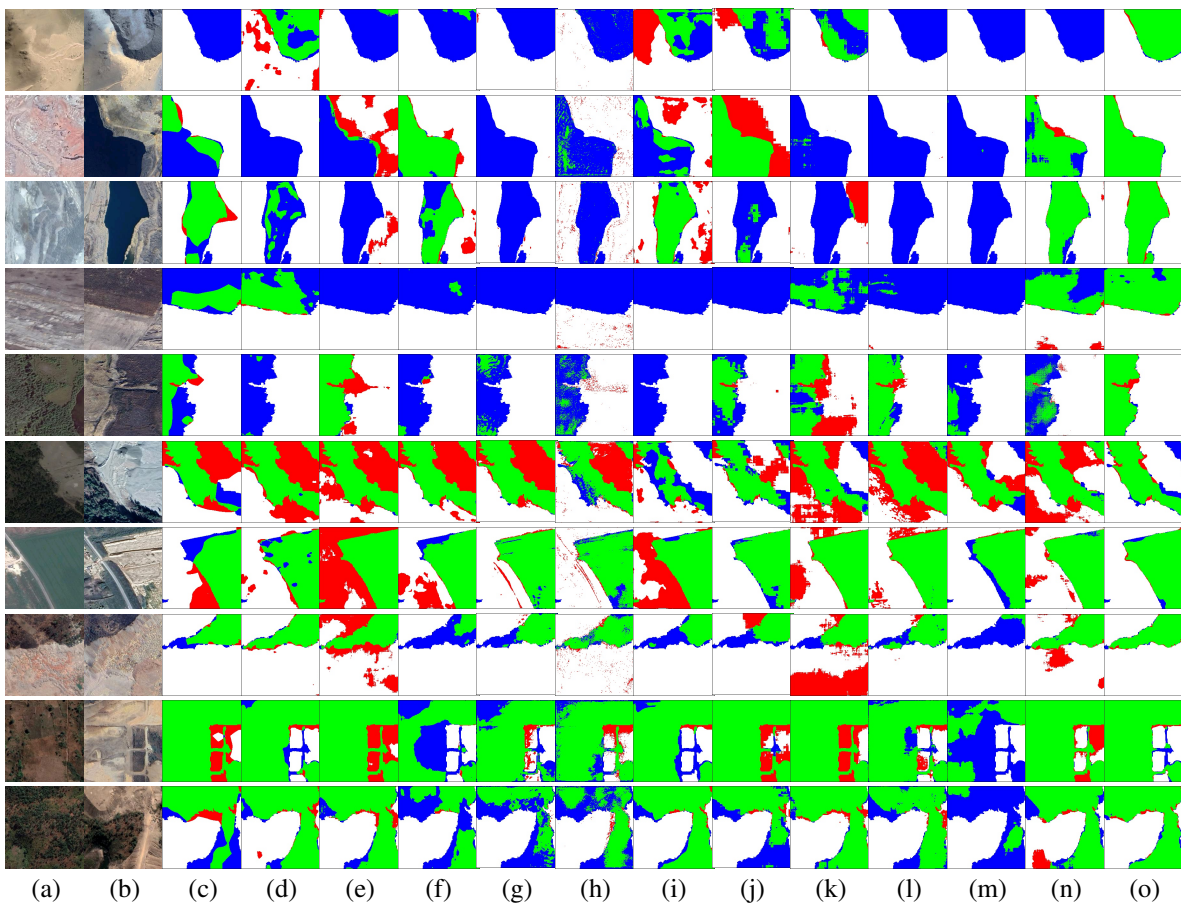


Figure 12: Visual comparisons of the proposed method and the state-of-the-art approaches on the MineNetCD dataset. (a) Pre-change images. (b) Post-change images. (c) A2Net. (d) BIT. (e) ChangeFormer. (f) DMINet. (g) FC-EF (h) FCNPP (i) ICIFNet (j) RDPNet (k) ResUnet (l) SiamUnet-Conc (m) SiamUnet-Diff (n) SNUNet (o) MineNetCD. The rendered colors represent true positives (green), true negatives (white), false positives (red), and false negatives (blue).

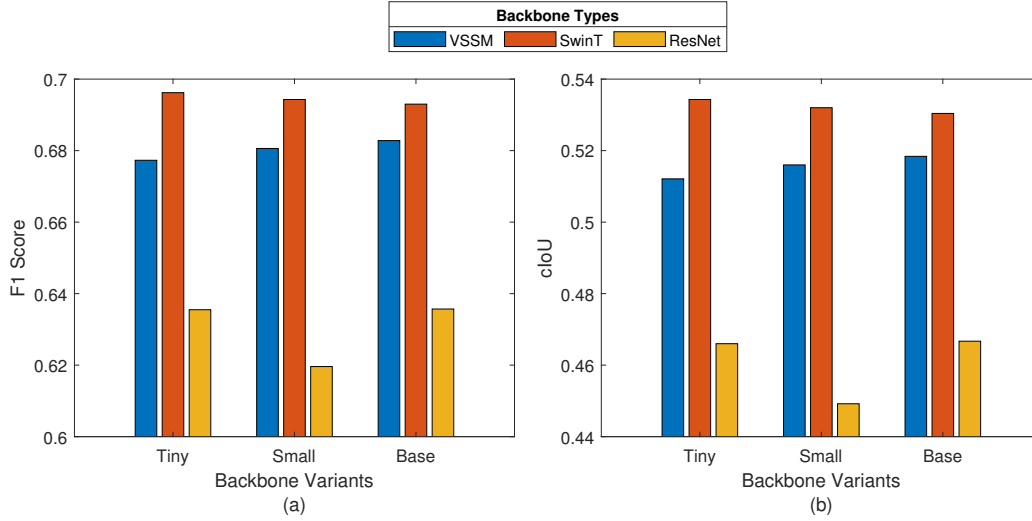


Figure 13: Comparison results of MineNetCD with different backbone models, including VMamba, Swin Transformer (SwinT), and ResNet on the MineNetCD dataset. The tiny, small, and base scales of the ResNet model indicate the ResNet-18, ResNet-50, and ResNet-101, respectively. (a) and (b) display the results in terms of F1 score and cIoU metrics, respectively.

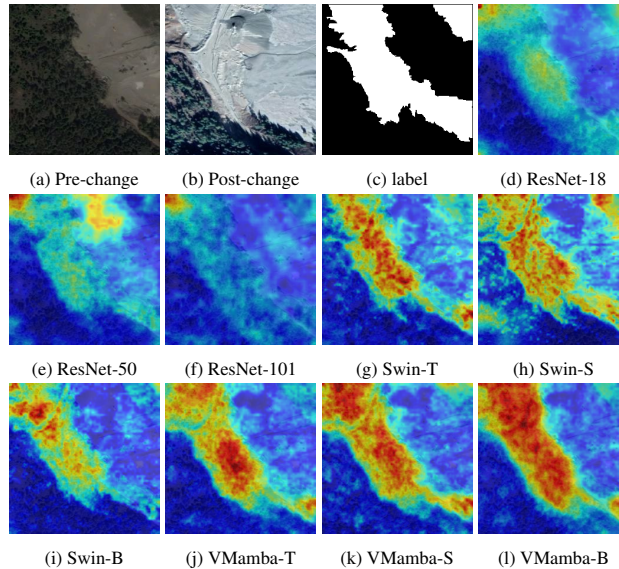


Figure 14: GradCAM visualizations of change-aware representations using different backbone variants on MineNetCD.

est performance is achieved by the Swin Transformer Tiny, indicating that the deep features extracted by a larger self-attention-based backbone may be too abstract to distinguish changes in MineNetCD.

Furthermore, we leverage the GradCAM [48] technique to visualize the change-aware representations of different backbone variants, as shown in Fig. 14. It can be observed that the ResNet variants cannot extract effective features among the changed areas, as shown on the label. Furthermore, the heatmaps of the change-aware representations generated by the VMamba series have over-smooth boundaries, which cannot precisely characterize the extent of changed areas. In contrast, the Swin Transformer series can precisely capture the change-aware representations with sharp boundaries, indicating its ability to process the bi-temporal RS images into effective features with the ChangeFFT module.

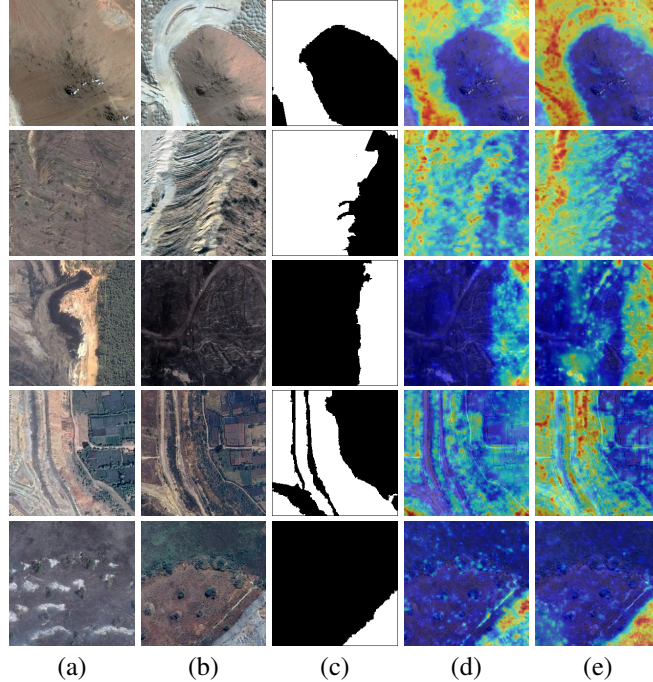


Figure 15: Comparison of GradCAM visualizations of feature differences and change-aware representations: (a) Pre-change images, (b) Post-change images, (c) labels, (d) Bi-temporal deep feature differences, and (e) Change-aware representations learned by ChangeFFT.

Table 3: Performance improvements of ChangeFFT module based on different backbone variants.

Backbones	Variants	F1	cIoU
VMamba	VMamba-S	+0.0163	+0.0184
	VMamba-T	+0.0055	+0.0061
	VMamba-B	+0.0234	+0.0262
Swin Transformer	Swin-T	+0.0340	+0.0389
	Swin-S	+0.0219	+0.0253
	Swin-B	+0.0226	+0.0258
ResNet	ResNet-18	+0.0098	+0.0106
	ResNet-50	+0.0098	+0.0100
	ResNet-101	+0.0085	+0.0089

## 5.7 Ablation studies

To evaluate the effectiveness of the ChangeFFT module, we conducted extensive ablation studies to build the MineNetCD model without using the ChangeFFT module. In this case, the multi-scale deep feature differences are directly fed into the UperNet-based change decoder to reconstruct a change map. Our experiments demonstrated that the ChangeFFT module improves performance in all settings based on various backbones, as shown in Table 3. In particular, incorporating the ChangeFFT module improves up to 3.40% F1 score and 3.89% cIoU based on the Swin Transformer base backbone. The ChangeFFT module is also effective on the VMamba series and ResNet series, indicating that the ChangeFFT module possesses superior compatibility and the potential to become a plug-and-play module in more change detection approaches.

We also display the GradCAM visualization to compare the conventional feature difference methods and the change-aware representations based on the Swin Tranformer base backbone, as shown in Fig. 15. It can be seen in the results that the ChangeFFT module significantly refines the feature difference and obtains change-aware representations highly focused on the changed areas. Specifically, the change-aware representations have a more accurate mapping of ground instances and reduce the noises within the feature differences.



## 6 Conclusion

In this article, we introduce MineNetCD, a comprehensive benchmark for global mining change detection aimed at promoting the sustainability goals of the extractive industry. MineNetCD involves a global mining change detection dataset, a change-aware fast Fourier transform (ChangeFFT) module-based baseline model, and a unified change detection (UCD) framework. The dataset includes bi-temporal high-resolution remote sensing images and pixel-level annotations of changed areas from 100 mining sites worldwide. Our baseline model, utilizing the ChangeFFT module, achieves better than state-of-the-art performance by enabling change-aware representation learning in the frequency domain. The UCD framework features over 70 pretrained models based on 5 change detection datasets, democratizing access to deep learning-based change detection methods without requiring specialized expertise.

With this work, we provide a robust solution for mining change detection, which is instrumental for environmental impact assessments in the mining industry using geospatial data. We anticipate that MineNetCD will pioneer advancements in sustainable metal sourcing and inspire future research focused on environmentally responsible mining practices.

## Acknowledgment

The authors would like to thank Mr. Yasong Shi and Mr. Yilong Deng for their efforts in building the MineNetCD dataset. This work was supported by the European Regional Development Fund and the Land of Saxony by providing the high specification Nvidia A100 GPU server that we used in our experiments.

## References

- [1] L. J. Sonter, D. Herrera, D. J. Barrett, G. L. Galford, C. J. Moran, and B. S. Soares-Filho, "Mining drives extensive deforestation in the brazilian amazon," *Nature communications*, vol. 8, no. 1, p. 1013, 2017.
- [2] S. Du, J. Xing, J. Li, S. Du, C. Zhang, and Y. Sun, "Open-pit mine extraction from very high-resolution remote sensing images using om-deeplab," *Natural Resources Research*, vol. 31, no. 6, pp. 3173–3194, 2022.
- [3] V. Maus, S. Giljum, J. Gutschlhofer, D. M. da Silva, M. Probst, S. L. Gass, S. Luckeneder, M. Lieber, and I. McCallum, "A global-scale data set of mining areas," *Scientific data*, vol. 7, no. 1, p. 289, 2020.
- [4] L. J. Sonter, M. C. Dade, J. E. Watson, and R. K. Valenta, "Renewable energy production will exacerbate mining threats to biodiversity," *Nature communications*, vol. 11, no. 1, p. 4174, 2020.
- [5] T. He, W. Xiao, Y. Zhao, X. Deng, and Z. Hu, "Identification of waterlogging in eastern china induced by mining subsidence: A case study of google earth engine time-series analysis applied to the huainan coal field," *Remote Sensing of Environment*, vol. 242, p. 111742, 2020. [Online]. Available: <https://www.sciencedirect.com/science/article/pii/S0034425720301127>
- [6] B. Chen, Z. Li, C. Yu, D. Fairbairn, J. Kang, J. Hu, and L. Liang, "Three-dimensional time-varying large surface displacements in coal exploiting areas revealed through integration of sar pixel offset measurements and mining subsidence model," *Remote Sensing of Environment*, vol. 240, p. 111663, 2020. [Online]. Available: <https://www.sciencedirect.com/science/article/pii/S0034425720300328>
- [7] R. Gloaguen, S. H. Ali, R. Herrington, L. Ajjabou, E. Downey, and I. S. Stewart, "Mineral revolution for the wellbeing economy," *Global Sustainability*, vol. 5, p. e15, 2022.
- [8] O. Renn, R. Gloaguen, C. Benighaus, L. Ajjabou, L. Benighaus, V. Del Rio, J. Gómez, S. Kauppi, M. Keßelring, M. Kirsch *et al.*, "Metal sourcing for a sustainable future," 2022.
- [9] J. Gallwey, C. Robiati, J. Coggan, D. Vogt, and M. Eyre, "A sentinel-2 based multispectral convolutional neural network for detecting artisanal small-scale mining in ghana: Applying deep learning to shallow mining," *Remote Sensing of Environment*, vol. 248, p. 111970, 2020. [Online]. Available: <https://www.sciencedirect.com/science/article/pii/S0034425720303400>
- [10] W. T. Witkowski, M. Łucka, A. Guzy, H. Sudhaus, A. Barańska, and R. Hejmanowski, "Impact of mining-induced seismicity on land subsidence occurrence," *Remote Sensing of Environment*, vol. 301, p. 113934, 2024. [Online]. Available: <https://www.sciencedirect.com/science/article/pii/S0034425723004868>
- [11] P. Ghamisi, K. R. Shahi, P. Duan, B. Rasti, S. Lorenz, R. Booyesen, S. Thiele, I. C. Contreras, M. Kirsch, and R. Gloaguen, "The potential of machine learning for a more responsible sourcing of critical raw materials," *IEEE Journal of Selected Topics in Applied Earth Observations and Remote Sensing*, vol. 14, pp. 8971–8988, 2021.

- [12] P. Ghamisi, W. Yu, A. Marinoni, C. M. Gevaert, C. Persello, S. Selvakumaran, M. Giroto, B. P. Horton, P. Rufin, P. Hostert *et al.*, “Responsible ai for earth observation,” *arXiv preprint arXiv:2405.20868*, 2024.
- [13] W. Li, J. Li, S. Du, C. Zhang, and J. Xing, “Multi-level difference network for change detection from very high-resolution remote sensing images: A case study in open-pit mines,” *Remote Sensing*, vol. 15, no. 14, p. 3482, 2023.
- [14] J. Li, J. Xing, S. Du, S. Du, C. Zhang, and W. Li, “Change detection of open-pit mine based on siamese multiscale network,” *IEEE Geoscience and Remote Sensing Letters*, vol. 20, pp. 1–5, 2023.
- [15] Z. Xie, J. Jiang, D. Yuan, K. Li, and Z. Liu, “Gan-based sub-instance augmentation for open-pit mine change detection in remote sensing images,” *IEEE Transactions on Geoscience and Remote Sensing*, vol. 62, pp. 1–19, 2024.
- [16] Z. Lv, T. Liu, J. A. Benediktsson, and N. Falco, “Land cover change detection techniques: Very-high-resolution optical images: A review,” *IEEE Geoscience and Remote Sensing Magazine*, vol. 10, no. 1, pp. 44–63, 2021.
- [17] W. Shi, M. Zhang, R. Zhang, S. Chen, and Z. Zhan, “Change detection based on artificial intelligence: State-of-the-art and challenges,” *Remote Sensing*, vol. 12, no. 10, p. 1688, 2020.
- [18] Y. Lin, S. Li, L. Fang, and P. Ghamisi, “Multispectral change detection with bilinear convolutional neural networks,” *IEEE Geoscience and Remote Sensing Letters*, vol. 17, no. 10, pp. 1757–1761, 2020.
- [19] Z. Li, F. Lu, H. Zhang, L. Tu, J. Li, X. Huang, C. Robinson, N. Malkin, N. Jovic, P. Ghamisi, R. Hänsch, and N. Yokoya, “The outcome of the 2021 ieee grss data fusion contest—track msd: Multitemporal semantic change detection,” *IEEE Journal of Selected Topics in Applied Earth Observations and Remote Sensing*, vol. 15, pp. 1643–1655, 2022.
- [20] S. Chang, M. Kopp, P. Ghamisi, and B. Du, “Dsfer-net: A deep supervision and feature retrieval network for bitemporal change detection using modern hopfield networks,” 2024.
- [21] C. Zhang, P. Yue, D. Tapete, L. Jiang, B. Shangguan, L. Huang, and G. Liu, “A deeply supervised image fusion network for change detection in high resolution bi-temporal remote sensing images,” *ISPRS Journal of Photogrammetry and Remote Sensing*, vol. 166, pp. 183–200, 2020.
- [22] S. Fang, K. Li, J. Shao, and Z. Li, “Snunet-cd: A densely connected siamese network for change detection of vhr images,” *IEEE Geoscience and Remote Sensing Letters*, vol. 19, pp. 1–5, 2021.
- [23] Y. Feng, J. Jiang, H. Xu, and J. Zheng, “Change detection on remote sensing images using dual-branch multilevel intertemporal network,” *IEEE Transactions on Geoscience and Remote Sensing*, vol. 61, pp. 1–15, 2023.
- [24] Q. Shi, M. Liu, S. Li, X. Liu, F. Wang, and L. Zhang, “A deeply supervised attention metric-based network and an open aerial image dataset for remote sensing change detection,” *IEEE transactions on geoscience and remote sensing*, vol. 60, pp. 1–16, 2021.
- [25] X. Peng, R. Zhong, Z. Li, and Q. Li, “Optical remote sensing image change detection based on attention mechanism and image difference,” *IEEE Transactions on Geoscience and Remote Sensing*, vol. 59, no. 9, pp. 7296–7307, 2020.
- [26] H. Chen, Z. Qi, and Z. Shi, “Remote sensing image change detection with transformers,” *IEEE Transactions on Geoscience and Remote Sensing*, vol. 60, pp. 1–14, 2021.
- [27] D. Hong, B. Zhang, X. Li, Y. Li, C. Li, J. Yao, N. Yokoya, H. Li, P. Ghamisi, X. Jia, A. J. Plaza, P. Gamba, J. A. Benediktsson, and J. Chanussot, “Spectralgpt: Spectral remote sensing foundation model,” 2023. [Online]. Available: <https://api.semanticscholar.org/CorpusID:267628000>
- [28] W. G. C. Bandara and V. M. Patel, “A transformer-based siamese network for change detection,” in *IGARSS 2022-2022 IEEE International Geoscience and Remote Sensing Symposium*. IEEE, 2022, pp. 207–210.
- [29] X. Zhang, W. Yu, and M.-O. Pun, “Multilevel deformable attention-aggregated networks for change detection in bitemporal remote sensing imagery,” *IEEE Transactions on Geoscience and Remote Sensing*, vol. 60, pp. 1–18, 2022.
- [30] C. Zhang, L. Wang, S. Cheng, and Y. Li, “Swinsunet: Pure transformer network for remote sensing image change detection,” *IEEE Transactions on Geoscience and Remote Sensing*, vol. 60, pp. 1–13, 2022.
- [31] W. Li, L. Xue, X. Wang, and G. Li, “Convtransnet: A cnn–transformer network for change detection with multiscale global–local representations,” *IEEE Transactions on Geoscience and Remote Sensing*, vol. 61, pp. 1–15, 2023.
- [32] W. Liu, Y. Lin, W. Liu, Y. Yu, and J. Li, “An attention-based multiscale transformer network for remote sensing image change detection,” *ISPRS Journal of Photogrammetry and Remote Sensing*, vol. 202, pp. 599–609, 2023.

- [33] W. Yu, X. Zhang, S. Das, X. X. Zhu, and P. Ghamisi, "Maskcd: A remote sensing change detection network based on mask classification," *arXiv preprint arXiv:2404.12081*, 2024.
- [34] H. Chen and Z. Shi, "A spatial-temporal attention-based method and a new dataset for remote sensing image change detection," *Remote Sensing*, vol. 12, no. 10, p. 1662, 2020.
- [35] K. He, X. Zhang, S. Ren, and J. Sun, "Deep residual learning for image recognition," in *Proceedings of the IEEE conference on computer vision and pattern recognition*, 2016, pp. 770–778.
- [36] Z. Liu, Y. Lin, Y. Cao, H. Hu, Y. Wei, Z. Zhang, S. Lin, and B. Guo, "Swin transformer: Hierarchical vision transformer using shifted windows," in *Proceedings of the IEEE/CVF international conference on computer vision*, 2021, pp. 10 012–10 022.
- [37] L. Zhu, B. Liao, Q. Zhang, X. Wang, W. Liu, and X. Wang, "Vision mamba: Efficient visual representation learning with bidirectional state space model," *arXiv preprint arXiv:2401.09417*, 2024.
- [38] Z. Qin, P. Zhang, F. Wu, and X. Li, "Fcanet: Frequency channel attention networks," in *Proceedings of the IEEE/CVF international conference on computer vision*, 2021, pp. 783–792.
- [39] T. Xiao, Y. Liu, B. Zhou, Y. Jiang, and J. Sun, "Unified perceptual parsing for scene understanding," in *Proceedings of the European conference on computer vision (ECCV)*, 2018, pp. 418–434.
- [40] Z. Li, C. Tang, X. Liu, W. Zhang, J. Dou, L. Wang, and A. Y. Zomaya, "Lightweight remote sensing change detection with progressive feature aggregation and supervised attention," *IEEE Transactions on Geoscience and Remote Sensing*, vol. 61, pp. 1–12, 2023.
- [41] R. C. Daudt, B. Le Saux, and A. Boulch, "Fully convolutional siamese networks for change detection," in *2018 25th IEEE International Conference on Image Processing (ICIP)*. IEEE, 2018, pp. 4063–4067.
- [42] T. Lei, Y. Zhang, Z. Lv, S. Li, S. Liu, and A. K. Nandi, "Landslide inventory mapping from bitemporal images using deep convolutional neural networks," *IEEE Geoscience and Remote Sensing Letters*, vol. 16, no. 6, pp. 982–986, 2019.
- [43] Y. Feng, H. Xu, J. Jiang, H. Liu, and J. Zheng, "Icif-net: Intra-scale cross-interaction and inter-scale feature fusion network for bitemporal remote sensing images change detection," *IEEE Transactions on Geoscience and Remote Sensing*, vol. 60, pp. 1–13, 2022.
- [44] H. Chen, F. Pu, R. Yang, R. Tang, and X. Xu, "Rdp-net: Region detail preserving network for change detection," *IEEE Transactions on Geoscience and Remote Sensing*, vol. 60, pp. 1–10, 2022.
- [45] L. Yuan, Y. Li, Y. Si, J. Ren, Y. Yang, Y. Gong, Y. Xia, Z. Tong, and L. Tong, "Multi-objects change detection based on res-unet," in *2021 IEEE International Geoscience and Remote Sensing Symposium IGARSS*, 2021, pp. 4364–4367.
- [46] T. Wolf, L. Debut, V. Sanh, J. Chaumond, C. Delangue, A. Moi, P. Cistac, T. Rault, R. Louf, M. Funtowicz, J. Davison, S. Shleifer, P. von Platen, C. Ma, Y. Jernite, J. Plu, C. Xu, T. L. Scao, S. Gugger, M. Drame, Q. Lhoest, and A. M. Rush, "Transformers: State-of-the-art natural language processing," in *Proceedings of the 2020 Conference on Empirical Methods in Natural Language Processing: System Demonstrations*. Online: Association for Computational Linguistics, Oct. 2020, pp. 38–45. [Online]. Available: <https://www.aclweb.org/anthology/2020.emnlp-demos.6>
- [47] S. Gugger, L. Debut, T. Wolf, P. Schmid, Z. Mueller, S. Mangrulkar, M. Sun, and B. Bossan, "Accelerate: Training and inference at scale made simple, efficient and adaptable." <https://github.com/huggingface/accelerate>, 2022.
- [48] R. R. Selvaraju, M. Cogswell, A. Das, R. Vedantam, D. Parikh, and D. Batra, "Grad-cam: Visual explanations from deep networks via gradient-based localization," in *Proceedings of the IEEE international conference on computer vision*, 2017, pp. 618–626.